

Characterization of scintillator-based detectors for few-ten-keV high-spatial-resolution x-ray imaging

Jakob C. Larsson,^{a)} Ulf Lundström, and Hans M. Hertz

Biomedical and X-ray Physics, Department of Applied Physics, KTH Royal Institute of Technology/Albanova, Stockholm 10691, Sweden

(Received 16 October 2015; revised 7 April 2016; accepted for publication 25 April 2016; published 9 May 2016)

Purpose: High-spatial-resolution x-ray imaging in the few-ten-keV range is becoming increasingly important in several applications, such as small-animal imaging and phase-contrast imaging. The detector properties critically influence the quality of such imaging. Here the authors present a quantitative comparison of scintillator-based detectors for this energy range and at high spatial frequencies.

Methods: The authors determine the modulation transfer function, noise power spectrum (NPS), and detective quantum efficiency for Gadox, needle CsI, and structured CsI scintillators of different thicknesses and at different photon energies. An extended analysis of the NPS allows for direct measurements of the scintillator effective absorption efficiency and effective light yield as well as providing an alternative method to assess the underlying factors behind the detector properties.

Results: There is a substantial difference in performance between the scintillators depending on the imaging task but in general, the CsI based scintillators perform better than the Gadox scintillators. At low energies (16 keV), a thin needle CsI scintillator has the best performance at all frequencies. At higher energies (28–38 keV), the thicker needle CsI scintillators and the structured CsI scintillator all have very good performance. The needle CsI scintillators have higher absorption efficiencies but the structured CsI scintillator has higher resolution.

Conclusions: The choice of scintillator is greatly dependent on the imaging task. The presented comparison and methodology will assist the imaging scientist in optimizing their high-resolution few-ten-keV imaging system for best performance. © 2016 American Association of Physicists in Medicine. [<http://dx.doi.org/10.1118/1.4948687>]

Key words: X-ray detector, scintillator, MTF, NPS, DQE

1. INTRODUCTION

Detector properties critically influence the image quality in x-ray imaging. Scintillator-based detectors are a key component in high-resolution laboratory-source imaging systems in the ten-to-few-ten keV energy range. In the present paper, we present a quantitative comparison of different scintillators for imaging in this energy range and at high spatial frequencies. The comparison is based on an extension of existing methods and relies on a detector system with exchangeable scintillators and a microfocus source suitable for high-resolution imaging.

High-resolution x-ray imaging in the few-ten-keV range is of interest for an extensive range of applications including small-animal imaging, mammography, and nondestructive testing of low Z materials. Although absorption is still the contrast mechanism dominating present systems, new modalities utilizing the phase shift of the x-rays are emerging. Such phase-contrast imaging^{1,2} shows promise for both high-spatial-resolution and low dose, and can be used with a compact polychromatic source. However, the successful implementation of phase-contrast imaging to, e.g., biomedical applications would benefit from reductions in exposure time, further reduction of dose and improved signal-to-noise ratio for improved observability of small details. Recent

development in high-brightness sources show promise to lift the source limitation for high-resolution imaging.^{3,4} Thus, the detector is currently a major limitation in such imaging systems.

Indirect detectors use a scintillator to convert x-ray photons into visible photons which are then detected conventionally, e.g., in a CCD. The scintillator has an intrinsic trade-off between high-spatial-resolution and low noise.⁵ Increasing the scintillator thickness improves detection efficiency and signal-to-noise ratio (SNR) but also reduces spatial resolution. Decreasing the thickness improves spatial resolution but reduces SNR. Several techniques to reduce this trade-off have been proposed, such as microcolumnar⁶ and structured^{7,8} scintillators. These techniques introduce structures in the scintillator that act as light guides for the visible-light, reducing the lateral spread and increasing resolution.

The performance of a detection system is quantitatively described by several parameters.^{9,10} We base the analysis in the present paper on the three most common, the modulation transfer function (MTF), noise power spectrum (NPS), and the detective quantum efficiency (DQE). The MTF gives a complete description of the spatial resolution for a translation invariant system. The NPS describes the noise levels at different spatial frequencies. The MTF and NPS can be

combined to form the DQE, which provides a spatial-frequency-resolved measure of the detector’s SNR² relative to the SNR² of an ideal photon-noise-limited detector.

Several scintillator-based detector systems have been evaluated quantitatively before. However, these previous studies focus on medical-imaging applications at higher energies^{11–13} and/or at low spatial resolution (<15 cycles/mm).^{14,15} In the present paper, we present a quantitative comparison of scintillators in terms of resolution, noise, and overall performance at energies in the few-ten-keV range with focus on high-spatial-resolution imaging (up to 37 cycles/mm). A range of unstructured, microcolumnar, and structured scintillators of varying thicknesses were measured to determine their MTF, NPS, and DQE as well as investigating more specific questions such as the thickness dependence and the efficiency of the different light-guiding techniques. Our method relies on the use of an indirect detector system with exchangeable scintillators, allowing for a fair comparison between the different scintillators independent of other system parameters, as well as a microfocus source suitable for high-resolution imaging. The MTF and NPS are measured by established methods, albeit applied to higher spatial frequencies than previously explored. An extended analysis of the NPS allows for direct measurements of the effective absorption efficiency and effective light yield of the scintillators and an alternative method to assess the detector properties.

2. MATERIALS AND METHODS

2.A. Experimental arrangement

Figure 1(a) shows the experimental arrangement. It consists of an x-ray source, the detector with its scintillator, and an opaque edge.

The source is a liquid-metal-jet anode x-ray microfocus tube (R5, Excillum), operating with a Ga/In/Sn alloy metal jet at an acceleration voltage of 50 kVp. The spot size is approximately 8 × 8 μm². Figure 1(b) shows the emitted spectrum (no filter, mean energy 16 keV) as well as the spectra after external filtering with 1 and 10 mm Al, resulting in mean energies of 28 and 38 keV, respectively. This corresponds to a first HVL of 0.43, 2.0, and 4.1 mm Al, respectively. All detectors were measured at these three energies. The spectra were measured with a photon-counting CdTe-based spectrometer (X-123CdTe, Amptek).

The detector is an indirect scintillator-based detector (PIXIS-XF 2048B, Princeton Instruments) with exchangeable scintillators placed 1 m from the source. The Peltier-cooled 2048 × 2048 pixel CCD is coupled 1:1 to the scintillator by a fiber optic plate (FOP). The pixel pitch and fill factor are 13.5 μm and 100%, respectively, giving the CCD an active area of 27.6 × 27.6 mm². The scintillators were placed directly on top of the FOP and pressed down to assure good contact. No optical coupling fluid was used but repeated measurements with different scintillator placements gave identical results.

Figure 1(c) depicts the scintillators investigated. The thicknesses were taken from the product data and the densities were measured from each scintillator’s absorption spectrum:

Gadox: This scintillator consists of unstructured Gd₂O₂S:Tb deposited on a 1 mm thick FOP with 6 μm diameter fibers (P43, Proxivision). They had a grain size of 2 μm, and an effective diameter of 42 μm. Three “Gadox” scintillators of thickness 10, 20, and 40 μm were investigated. The Gd₂O₂S:Tb densities in the three samples were measured to 4.75–4.81 g/cm³.

Needle CsI: This scintillator consists of microcolumnar CsI:Tl deposited on a 3 mm thick FOP with 6 μm diameter fibers (J6671-01, Hamamatsu). The effective area was

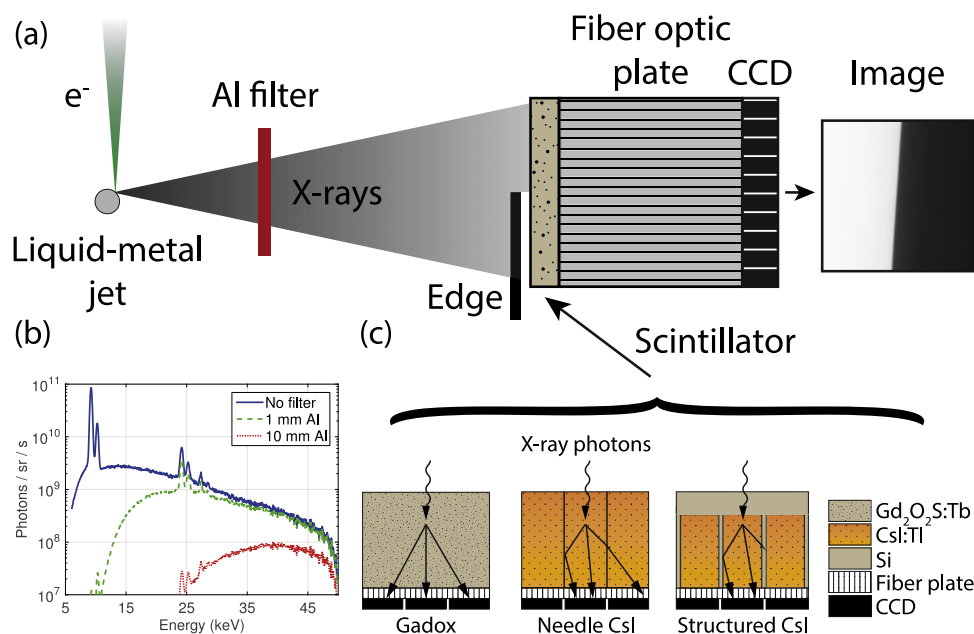


FIG. 1. (a) Experimental arrangement for measuring the MTF, NPS, and DQE. (b) Measurements were performed at three different source spectra with mean energies at 16, 28, and 38 keV. (c) Three different types of scintillators were investigated.

27 × 17 mm². Three “needle CsI” scintillators of thickness 50, 200, and 400 μm were investigated. The CsI densities were measured to 2.89–3.2 g/cm³, corresponding to packing densities of 60%–70% assuming a CsI density of 4.51 g/cm³. Similar packing densities have been reported previously.¹²

Structured CsI: The structured scintillator consists of 200 μm deep CsI(Tl)-filled wells etched into a 500 μm thick silicon substrate (S535, Scint-X). The hexagonal wells were filled by melting CsI(Tl) powder⁷ and had a pitch of 30.8 μm and a wall thickness of 2.3 μm, corresponding to a fill factor of 86%. The total active area was 27.6 × 26.3 mm². One “structured CsI” scintillator was investigated. The CsI density was 3.86 g/cm³.

2.B. MTF

The presampling MTF was measured using an edge method, following Ref. 16. A polished opaque edge (1.2 mm tungsten) is placed in the center of and in close proximity to the detector window (~8 mm in front of the scintillator) and aligned perpendicular to the optical axis with a laser. Images of the edge are then acquired for each of the three different x-ray energies and stored digitally for analysis. The exposure time varied between a few seconds to several hours, depending on scintillator and x-ray energy, in order for the images to be photon-noise limited and so that no smoothing was required in the analysis. To remove any nonuniformities that might be present in the CCD, scintillator, FOP, or x-ray beam, the images were offset and flat-field corrected before the analysis.

The analysis starts by calculating the angle θ of the edge relative to the CCD sampling matrix. First, the position of the edge in each row of the image is determined by fitting the intensity values of each row to an error function. A first-order polynomial fit to this position array yields the edge angle (typically approx. 3.5°). In the next step, all pixel values in the image are projected along the edge and binned into a subpixel-spaced 1D array perpendicular to the edge, giving the averaged oversampled edge spread function ESF(x).¹⁶ The line spread function, LSF(x), is then determined via numerical differentiation of the ESF.

Finally, the presampling MTF is calculated by taking the 1D discrete Fourier transform of the LSF and normalizing it to its zero frequency,

$$\text{MTF}(f) = \text{DFT}\{\text{LSF}(x)\}. \quad (1)$$

When a sufficiently long exposure time was used, no smoothing or other manipulation of the ESF or LSF was required.

2.C. NPS

The NPS is measured with a 2D Fourier-transform method.⁹ Two open-beam (i.e., no edge) images were acquired for each x-ray energy and scintillator. One of the images is flat-field corrected (divided) with the other in order to remove nonuniformities in gain between pixels. The exposure time was chosen long enough for the system to be photon-noise limited. The exposure ranged from 7 to 15000 mR.

In the first step of the analysis, the corrected image is split into nonoverlapping subregions of 256 × 256 pixels. The NPS is calculated for each subregion and then averaged to obtain the final 2D NPS.⁹ The increase in variance from the flat-field correction is corrected by an additional division by 2. The 1D NPS, NPS(f), is then calculated by radially binning the frequencies in the 2D NPS. The zero frequency is excluded since it cannot be accurately measured.⁹

In the next step, the NPS(f) is normalized to the SNR, q , of an ideal energy-integrating detector, i.e., a detector which absorbs all incident radiation and is only limited by photon-noise from the x-ray photons, to form

$$\text{NPS}_{\text{norm}}(f) = q^2 \frac{\text{NPS}(f)}{I^2}. \quad (2)$$

Here I is the average intensity over the full active area and q is calculated from the source spectrum as¹⁷

$$q^2 = \frac{(\int \phi(E)EdE)^2}{\int \phi(E)E^2dE}, \quad (3)$$

where $\phi(E)$ is the x-ray spectrum in number of photons per photon energy and detector pixel. This normalization provides a simple tool to evaluate a detector’s noise properties since an ideal detector will have a NPS_{norm} of 1.

2.D. DQE

The DQE is calculated directly from the MTF and NPS_{norm} following Ref. 9 as

$$\text{DQE}(f) = \frac{\text{MTF}^2(f)}{\text{NPS}_{\text{norm}}(f)}. \quad (4)$$

The MTF had a higher sampling frequency than the NPS and is therefore down-sampled before the calculation. The integrated DQE (IDQE) is calculated by integrating the DQE up to the Nyquist frequency,

$$\text{IDQE} = \int_0^{f_{\text{Ny}}} \text{DQE}(f)df. \quad (5)$$

The Nyquist frequency for the CCD, $f_{\text{Ny}} = (2 \cdot \text{pixel pitch})^{-1} = 37 \text{ mm}^{-1}$, was used for all scintillators.

2.E. Effective absorption efficiency and visible photon detection

Here we introduce an extended analysis of the NPS. The analysis allows for direct determination of the effective absorption efficiency and the detected visible photon light yield from the NPS_{norm}.

The NPS_{norm} is normalized so that an ideal detector would have NPS_{norm} = 1 at all frequencies. A nonideal detector will have higher noise and thus a value larger than 1. If only x-ray photon-noise was present and the detector absorbed all x-ray photons, the NPS_{norm} would be similar to the MTF². This is a consequence of the original (incident) white photon-noise being modulated by the MTF of the system.

Nonperfect absorption, Swank noise,¹⁸ and the Lubberts' effect¹⁹ will further increase this frequency dependent noise. In this approximation, the NPS_{norm} at the zero frequency is inversely proportional to the x-ray absorption efficiency, η , and Swank factor, A_S , as $NPS_{norm}(0) = DQE^{-1}(0) = (A_S\eta)^{-1}$.²⁰

However, photon-noise from the visible-light photons will also be present. This noise is not affected by the MTF and will therefore add a constant value to the NPS_{norm} . This constant is inversely proportional to the number of visible-light photons detected. At high enough frequencies, the MTF is zero and the frequency dependent noise vanishes, leaving only the noise from the visible-light photons. Thus, by subtracting this constant from the zero frequency, we can calculate the effective x-ray absorption efficiency of the scintillator as well as estimate the number of detected visible-light photons per absorbed x-ray photon, Eqs. (6) and (7). A detailed derivation of Eqs. (6) and (7) using a linear cascade model is available as supplementary material.²¹

The model assumes that the MTF is zero at the Nyquist frequency. Figure 2 shows that this assumption holds for all scintillators in this study. The model does not account for *K*-fluorescence emission and reabsorption in the scintillator material. However, the majority of the measurements were done with x-ray energies below the *K* absorption edge of the scintillator material ($K_{Cs} = 36.0$ keV, $K_I = 33.2$ keV, $K_{Ga} = 50.2$ keV) where these effects are not present. For photon energies above the *K*-edge, Eqs. (6) and (7) will overestimate the result with about 10%.^{22,23}

With this background, the effective absorption efficiency can be calculated as

$$\eta_{eff} = \frac{1}{NPS_{norm}(0) - NPS_{norm}(\infty)} \tag{6}$$

The effective absorption efficiency corresponds to the absorbed x-ray photons that actually contribute to the image quality. This is a more relevant parameter to the imaging scientist than the conventional absorption efficiency, corresponding to all absorbed x-ray photons, since losses in the scintillator subsequent to the absorption of the x-ray photon may result in reduced SNR (cf., Sec. 3.B).

Furthermore, the number of detected visible-light photons for each absorbed x-ray photon can approximately be determined by

$$N_{vis/x} = \frac{NPS_{norm}(0) - NPS_{norm}(\infty)}{NPS_{norm}(\infty)} \tag{7}$$

For comparison between different scintillators $N_{vis/x}$ has to be normalized to the mean energy of the absorbed x-ray spectrum. This cannot be determined directly from the NPS_{norm} but has to be modeled. This is discussed further in Sec. 3.B.

Since the zero frequency value could not be calculated directly, it was found by making a linear extrapolation from the NPS data up to 3.2 mm^{-1} . $NPS_{norm}(\infty)$ was approximated with the NPS_{norm} value at the Nyquist frequency, $f_{Ny} = (2 \cdot \text{pixel pitch})^{-1} = 37 \text{ mm}^{-1}$.

3. RESULTS AND DISCUSSION

3.A. MTF

Figure 2 shows the experimentally measured presampling MTF for all scintillators. Independent of x-ray energy, the $10 \mu\text{m}$ thick Gadox scintillator has the highest MTF at lower spatial frequencies and the $50 \mu\text{m}$ thick needle CsI scintillator has the highest MTF at higher frequencies. The crossover

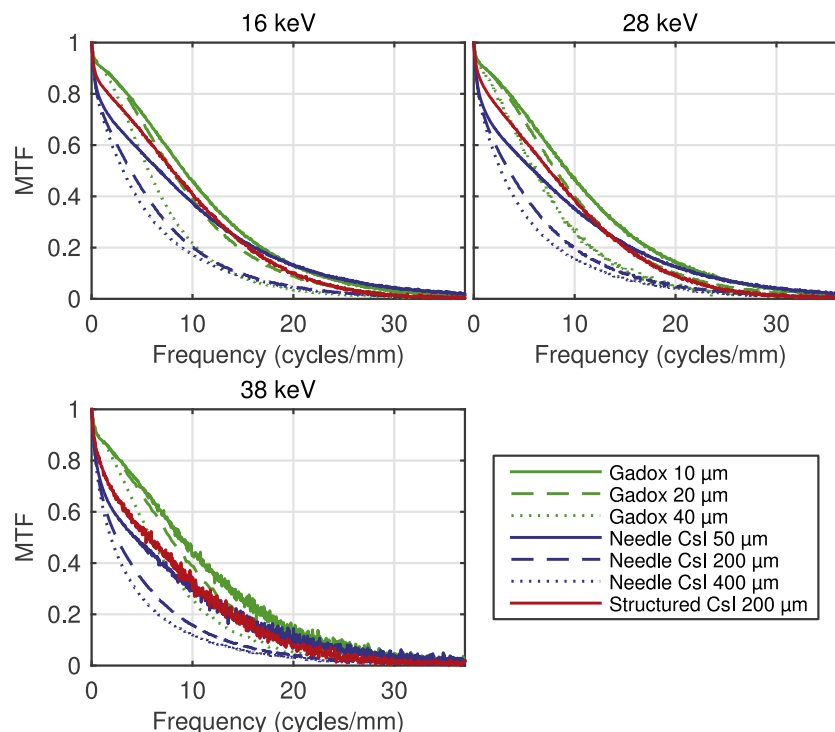


FIG. 2. The measured presampling MTF at three different energies.

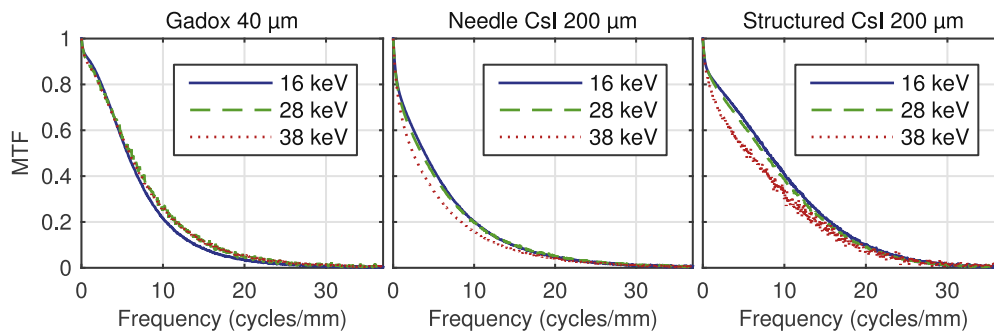


FIG. 3. The MTF at three different energies for one Gadox, one needle CsI, and one structured CsI scintillator.

frequency between the two increases with energy and is located at 20, 26, and 30 mm^{-1} for 16, 28, and 38 keV, respectively. The 200 and 400 μm needle CsI scintillators exhibit the lowest MTF. As for the thickness dependence, the MTF for each scintillator type decreases with increased thickness as expected. However, the difference between the 200 and 400 μm needle scintillators is very small despite the 200 μm difference in thickness. This has been observed previously.¹² The Gadox and needle CsI scintillators have FOP substrates of different thicknesses (1 and 3 mm, respectively) but this will not influence the MTF.^{24,25}

Comparing the two types of CsI-based scintillators, the 200 μm structured CsI scintillator performs a lot better than its 200 μm needle counterpart. At all three x-ray energies, it demonstrates 1.5 \times higher MTF at 5 mm^{-1} and about 2 \times higher MTF at 15 mm^{-1} . This indicates that the hexagonal wells are better at channeling the visible-light compared to the needle-like structures. The 200 μm structured scintillator is comparable to the 50 μm needle scintillator, slightly higher MTF for low frequencies and somewhat lower at higher frequencies.

As for the energy dependence, Fig. 3 displays the MTF for one scintillator of each type at three different x-ray energies. We note that the MTF increases slightly with energy for the Gadox scintillator but decreases with energy for the CsI-based scintillators. This difference is believed to be due to the different structures and materials of the scintillators. The Gadox scintillator is unstructured so the visible-light spreads basically isotropically inside the scintillator. Given that the average interaction depth of the x-ray photons will increase with energy and thereby move the interaction point closer to the CCD, the higher energies will result in increased resolution. The CsI scintillator on the other hand has internal

structures to channel the visible-light and is therefore less affected by the interaction depth. The reduction of the MTF for the CsI scintillator at 38 keV can be explained from its material composition. Cs and I have their K_{α} absorption edges at 36.0 and 33.2 keV, respectively. When the energy of the spectrum is higher, K_{α} fluorescence will be generated from both Cs and I, decreasing the resolution. The Gadox scintillator does not experience this since its K_{α} absorption edge lies at 50.2 keV. The same pattern is seen for all Gadox and CsI-based scintillators investigated in this paper.

From repeated measurements, we estimate that the uncertainty in the MTF is less than 5% below 30 cycles/mm and somewhat larger above that.

Figure 4 depicts a Siemens star imaged with one scintillator of each type. This illustrates a disadvantage of the structured CsI scintillator: The object is sampled in the hexagonal wells which have a larger pitch than the CCD pixel array. This causes a Moiré pattern to form at a spatial frequency observable in the Siemens star. The Nyquist frequency is 16.2 and 37.0 cycles/mm for the hexagonal wells and the CCD, respectively.

3.B. NPS

Figure 5 shows the measured $\text{NPS}_{\text{norm}}(f)$ for all scintillators at all three x-ray energies. From these data we extract $\text{NPS}_{\text{norm}}(0)$ and $\text{NPS}_{\text{norm}}(\infty)$ and directly determine the effective absorption efficiency with Eq. (6). Table I shows the results.

The effective absorption efficiency of Table I is directly determined from the measurement of the quantitative noise properties in the NPS for each individual scintillator. Thus, column “ η_{eff} ” in Table I depicts the absorption that directly

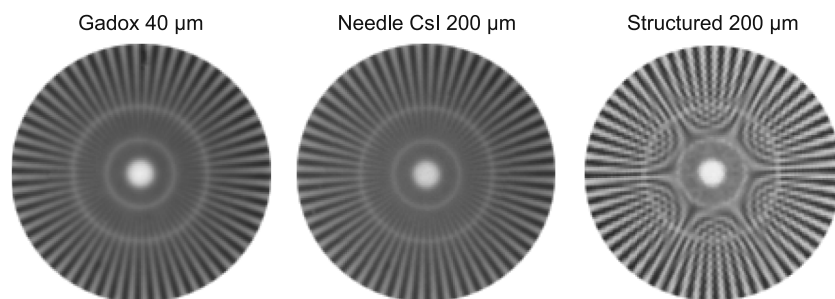


FIG. 4. A Siemens star imaged at 16 keV with one scintillator of each type. The spatial frequencies are 10 cycles/mm at the outer edge and 20 and 40 cycles/mm at the outer and inner bright ring, respectively.

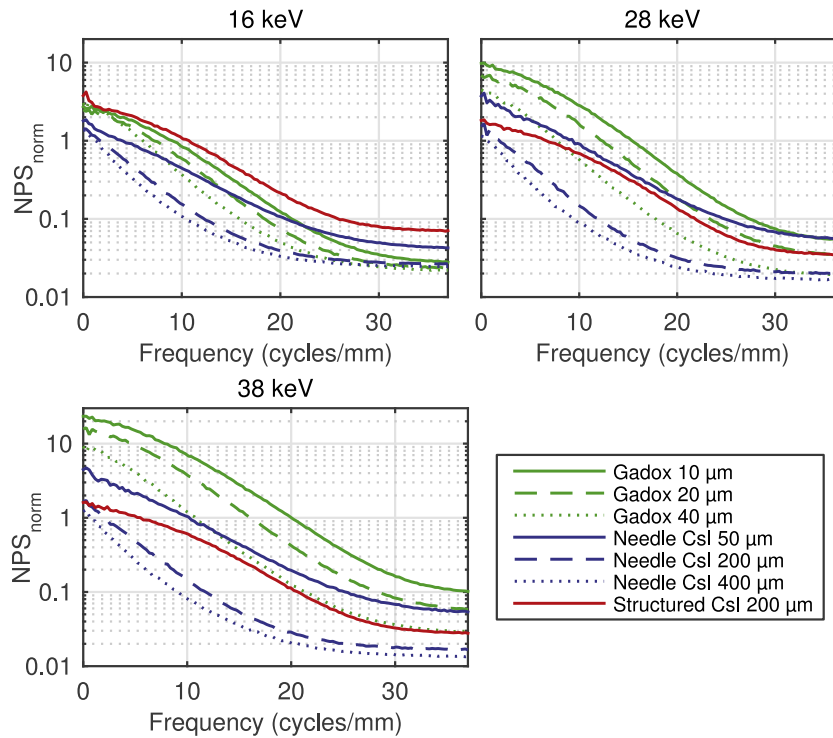


FIG. 5. The normalized NPS for all scintillators at three different energies.

contributes to the image quality. As stated above, this is a more relevant measure for the imaging scientist than the conventional absorption efficiency since losses in the scintillator may reduce the achievable SNR (cf. below). For comparison, we have included the conventional x-ray photon absorption efficiencies as determined by a classical method assuming Beer–Lambert’s law (column “ η_{cl} ”). Here, the thicknesses and attenuation coefficients were taken from the product data and the literature, respectively, while the densities were measured from each scintillator’s absorption spectrum. For Gadox and needle-grown CsI, we also introduced a more complex model taking the unequal light propagation from different depths, i.e., the optical component of Swank noise, into account (column “ η_{corr} ”). This model is described in detail in the Appendix and is based on Refs. 26–28 and Refs. 29 and 30 for Gadox and CsI, respectively.

In general, Table I confirms expected trends: Higher photon energy results in lower absorption efficiency and larger scintillator thickness results in increased absorption efficiency. The effective absorption efficiency obtained from the NPS_{norm} measurements typically follows the conventionally calculated data. However, for Gadox and needle CsI, the depth dependent loss of visible-light photons reduces the absorption efficiency with increasing scintillator thickness and lower energy. Most of the lower-energy x-ray photons are absorbed in the upper part of the scintillator, causing a larger fraction of the generated visible-light to be lost. The high-energy photons of the spectrum have a more uniform absorption profile in the scintillator and, thus, relatively less visible-photon losses. Thereby the higher-energy fraction with its higher relative noise receives a higher weight, increasing the $NPS_{norm}(0)$ and reducing the effective absorption efficiency. This effect is less apparent in

TABLE I. Scintillator absorption efficiency at different energies. For each energy, the effective absorption efficiency (η_{eff}), the classical photon absorption efficiency (η_{cl}), and the photon absorption efficiency corrected for scattering (η_{corr}) are shown.

| Scintillator (μm) | Scintillator absorption efficiency (%) | | | | | | | | |
|--------------------------------|--|-------------|---------------|--------------|-------------|---------------|--------------|-------------|---------------|
| | 16 keV | | | 28 keV | | | 38 keV | | |
| | η_{eff} | η_{cl} | η_{corr} | η_{eff} | η_{cl} | η_{corr} | η_{eff} | η_{cl} | η_{corr} |
| Gadox 10 | 37 | 40 | 37 | 10 | 9.9 | 8.6 | 4.3 | 3.6 | 3.1 |
| Gadox 20 | 40 | 58 | 45 | 15 | 19 | 15 | 6.4 | 7.0 | 5.7 |
| Gadox 40 | 33 | 69 | 39 | 22 | 32 | 24 | 11 | 14 | 10 |
| Needle CsI 50 | 57 | 58 | 58 | 27 | 25 | 23 | 23 | 23 | 22 |
| Needle CsI 200 | 71 | 80 | 72 | 67 | 67 | 62 | 61 | 66 | 63 |
| Needle CsI 400 | 75 | 87 | 78 | 88 | 86 | 79 | 83 | 86 | 81 |
| Structured CsI 200 | 27 | 24 | | 57 | 50 | | 65 | 58 | |

the structured CsI, mainly due to its substrate absorbing a large fraction of the lower-energy photons. Adding modeling of this effect to the conventional absorption data for the Gadox and needle CsI gives good agreement with the measured data.

At the higher energies (28 and 38 keV), the absorption efficiency for Gadox decreases rapidly with energy, where, e.g., the 10 μm Gadox absorption at 38 keV is $8.6\times$ and $2.3\times$ less than at 16 and 28 keV, respectively. The CsI behaves differently. Due to the Cs and I K_α absorption edges (36.0 and 33.2 keV respectively), the CsI scintillators have approximately the same absorption efficiency at 28 and 38 keV. However, since the models does not take K -fluorescence emission and reabsorption into account the absorption efficiencies at 38 keV will be slightly overestimated (cf. Sec. 2.E).

In contrast to the other scintillators, the absorption efficiency of the structured CsI scintillator increases with energy. At 16 keV, it is only 27%. Here the 300 μm thick silicon substrate absorbs a large fraction of the incident low-energy photons. As expected, substrate absorption decreases with higher energy and we measure approximately the same effective absorption efficiency at 28 and 38 keV as its 200 μm needle CsI counterpart. For the structured CsI, however, the thickness of the hexagonal wells sets an upper limit on the absorption efficiency. A wall thickness of 2.3 μm corresponds to a fill factor of 86% which, thus, will be the theoretical limit for the absorption efficiency.

The number of visible-light photons generated per x-ray photon, $N_{\text{vis}/x}$, was calculated from Eq. (7). Note that these values correspond to the number of detected photons, not the actual number generated by each x-ray photon. Since all measurements were made with the same system with equal internal losses and both Gadox and CsI have very similar

light yields (60 and 66 ph/keV, respectively),³¹ the relative numbers should allow for an accurate comparison between the scintillators. However, to make the comparison, $N_{\text{vis}/x}$ has to be normalized to the mean energy of the absorbed x-ray spectrum. This cannot be measured directly from the NPS_{norm} but has to be modeled. Using a simple model including Beer–Lambert’s law and the models in the Appendix, the average number of detected visible-light photons per keV for each scintillator material was calculate to 7.1 ph/keV for Gadox, 2.6 ph/keV for needle CsI, and 1.8 ph/keV for the structured CsI, i.e., there is a considerable difference between Gadox and needle CsI. This is expected since the light output of the needle CsI scintillators is reported to be 60% lower compared to a conventional phosphor screen.³² Both the Gadox and needle CsI scintillators also have FOP substrates which absorb up to 35% of the visible-light.³³ The structured CsI does not have a FOP substrate but still has the lowest value due to losses in the hexagonal wells. Finally we note that the $\text{NPS}_{\text{norm}}(f)$ will have an intrinsic uncertainty due to photon-noise and that $\text{NPS}_{\text{norm}}(0)$ will have an additional uncertainty due to the extrapolation. This will also introduce an uncertainty to the calculated effective absorption efficiencies and to the number of detected visible-light photons. From repeated measurements we estimate the uncertainty in the zero-frequency value to 10%–20% while the high-frequency uncertainty is considerably less, typically less than 5%.

3.C. DQE

Figure 6 shows the calculated DQE for all scintillators and Table II lists the IDQE, as determined from Eqs. (4) and (5), respectively.

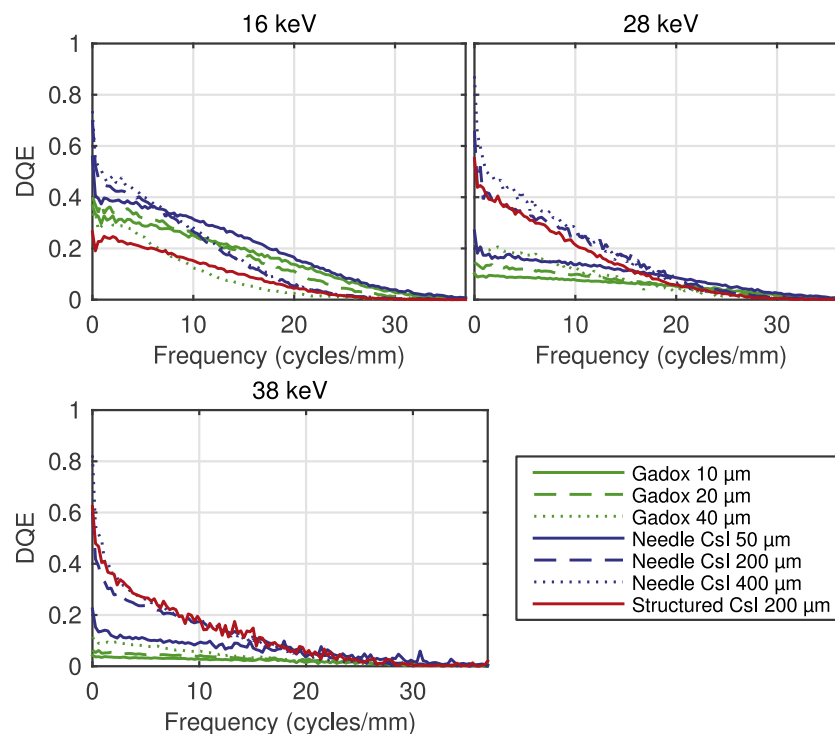


FIG. 6. The DQE measured for all scintillators at three different energies.

TABLE II. The integrated DQE at three different energies (highest values in bold).

| Scintillator (μm) | IDQE (mm^{-1}) | | |
|--------------------------------|---------------------------|------------|------------|
| | 16 keV | 28 keV | 38 keV |
| Gadox 10 | 5.8 | 2.0 | 0.74 |
| Gadox 20 | 5.5 | 2.3 | 0.95 |
| Gadox 40 | 3.1 | 2.7 | 1.3 |
| Needle CsI 50 | 7.2 | 3.4 | 2.3 |
| Needle CsI 200 | 5.7 | 5.6 | 4.0 |
| Needle CsI 400 | 6.0 | 6.1 | 4.3 |
| Structured CsI 200 | 3.2 | 4.9 | 4.4 |

At 16 keV, the 50 μm needle CsI scintillator has the highest DQE at higher frequencies ($>7 \text{ mm}^{-1}$) and also the highest IDQE. The 200 and 400 μm needle scintillators have an equally high DQE at lower frequencies but gets gradually less attractive at higher frequencies due to the lower resolution. The 10 and 20 μm thick Gadox scintillators have a very similar DQE over all frequencies and perform better than the 200 and 400 μm needle scintillators for frequencies over 13 mm^{-1} . The 40 μm thick Gadox scintillator has a comparatively low overall performance at all energies. The structured CsI scintillator also has a low DQE at 16 keV, mainly because the high absorption in the substrate decreases the absorption efficiency.

At 28 keV, the 50 μm needle CsI drops a factor 2 at low frequencies, but still has the highest DQE for frequencies above 20 mm^{-1} . Instead, the 400 μm needle scintillator has the best performance at the lower frequencies and also has the best overall performance. All three Gadox scintillators perform less well at all frequencies. The DQE for the structured scintillator, however, increases considerably compared to at 16 keV due to lower absorption in the substrate.

At 38 keV and for frequencies below 20 cycles/mm, the highest DQE and best overall performance is demonstrated by the 400 μm needle scintillator and 200 μm structured scintillator, closely followed by the 200 μm needle scintillator. The 50 μm needle scintillator drops slightly but is still better than all three Gadox scintillators. For spatial frequencies above 20 cycles/mm, however, the 50 μm needle scintillator has the highest DQE. This is due to a combination of a high MTF and relatively low noise.

The uncertainty in the present data is difficult to estimate accurately and varies with spatial frequency. However, given the $<5\%$ uncertainty in the MTF and the 10% – 20% in the NPS measurements, we estimate that the uncertainty in the DQE is typically less than 20% . We do not expect these errors to change the main conclusion above.

4. CONCLUSIONS

We have investigated the performance of several scintillators of different types and thicknesses at energies in the few-ten-keV range with focus on high-resolution imaging. Our study provides quantitative measurements of the MTF, NPS and DQE up to high spatial frequencies (37 cycles/mm)

and at different energies. The results allow for an overall quantitative comparison between the scintillators as well as studies of underlying details, e.g., absorption efficiency, thickness dependence, and the influence of different light guiding techniques. For this, the extended analysis of the normalized NPS providing the scintillators' effective absorption efficiency is important since it provides relevant data by direct measurements without the need for assumption of conventional methods. The methodology is applicable to a wide range of detector systems.

The results show large differences in the MTF, NPS, and DQE for different scintillators and energies but also confirm expected trends. Such expected behavior includes that increasing scintillator thickness reduces the resolution and the relative noise for each scintillator type, and that thin scintillators have a good performance at low energies but get gradually less attractive at higher energies due to the reduced absorption efficiency. Measurements also confirm that the structured CsI scintillator is the most efficient in reducing the diffusion of light inside the scintillator, albeit at the cost of lower absorption efficiency and less light throughput.

The large differences in MTF, NPS, and DQE observed indicate that the scintillator parameters should be chosen carefully given the imaging task and imaging system. One central system parameter is the energy. For imaging of a few-mm thick biosamples, 16 keV is typically fine, while thicker samples like, e.g., rodents and rats, require higher energy. Here, the 50 μm needle CsI scintillator has the best performance at low energies with highest DQE at all frequencies. At higher energies, the 200 and 400 μm needle CsI scintillators and the 200 μm structured CsI scintillator all have very good overall performance. The two needle CsI scintillators have higher absorption efficiency while the structured CsI scintillator has higher resolution. Again, it depends on the energy which scintillator and thickness that should be chosen.

ACKNOWLEDGMENTS

The authors thank Ulrich Vogt and Daniel Nilsson for discussions, and Scint-X for providing us with one of their scintillators. This work was supported by the Swedish Research Council, the Wallenberg Foundation, and the Stellenbosch Institute for Advanced Study.

CONFLICT OF INTEREST DISCLOSURE

The authors have no COI to report.

APPENDIX: LIGHT TRANSMISSION EFFICIENCY MODEL

1. Effective absorption efficiency

The effective absorption efficiency calculated from the NPS_{norm} [Eq. (6)] can be theoretically calculated from the source spectrum as

$$\eta = \frac{q^2}{q'^2} = \frac{\left(\int \phi(E)A(E)E dE\right)^2}{\int \phi(E)A(E)E^2 dE} = \frac{\left(\int \phi(E)A(E)E dE\right)^2}{\int \phi(E)E^2 dE}, \tag{A1}$$

where q^2 is the SNR² of an ideal detector [Eq. (3)], q'^2 is the SNR² of a real detector, $\phi(E)$ is the number of x-ray photons with energy E , and $A(E)$ is the absorption efficiency (according to Beer-Lambert’s law) at each energy. Since the nominator in the rightmost term of Eq. (A1) is weighted with respect to E and the denominator is weighted with respect to E^2 , the effective absorption efficiency is approximately the same as the photon absorption efficiency.

Taking the scattering of visible-light photons into account, the expression for q'^2 needs to be adjusted to include the depth of interaction. For visible-light photons generated in a dx thick layer at depth x , the adjusted expression for q'^2 can then be written as

$$q'^2 = \frac{\left(\int_{E_{\min}}^{E_{\max}} \int_0^T \phi(E)\mu(E)e^{-\mu(E)x}EG(x,T) dx dE\right)^2}{\int_{E_{\min}}^{E_{\max}} \int_0^T \phi(E)\mu(E)e^{-\mu(E)x}(EG(x,T))^2 dx dE}. \tag{A2}$$

Here, $\mu(E)$ is the attenuation coefficient, T is the thickness of the scintillator, and $G(x,T)$ is the light emission efficiency of the scintillator.

2. Turbulent phosphor scintillator

The light emission efficiency for a turbulent phosphor scintillator is given by^{27,28}

$$G(x,T) = \frac{\rho_1[(\beta + \rho_0)e^{\sigma x} + (\beta - \rho_0)e^{-\sigma x}]}{(\beta + \rho_0)(\beta + \rho_1)e^{\sigma T} - (\beta - \rho_0)(\beta - \rho_1)e^{-\sigma T}}. \tag{A3}$$

ρ_i is calculated from the reflectivities of the front and back surfaces of the scintillator,

$$\rho_i = \frac{1 - r_i}{1 + r_i}, \tag{A4}$$

and β and σ are two parameters related to the absorption and scattering of the visible-light photons inside the scintillator. The values of β and σ were taken from previous publications ($\beta = 0.03$ and $\sigma = 30 \text{ cm}^2/\text{g}$),²⁶ and ρ_0 and ρ_1 were set to 0.85 and 1, respectively.

3. Microcolumnar CsI scintillator

Following the model of Refs. 29 and 30, the light emission efficiency for a microcolumnar CsI scintillator was calculated as

$$G(x,T) = \frac{1}{2}(1 - R_1) \frac{k_T^{a(T-x)} + R_2 k_T^{a(T+x)}}{1 - k_T^{2aT} R_1 R_2}, \tag{A5}$$

where k_T is the loss of visible-light in a $1 \mu\text{m}$ thick scintillator layer and $a = 10^6 \text{ m}^{-1}$. k_T was fitted to the measured data and found to be 0.991, 0.996, and 0.998 for the 50, 200, and 400 μm thick scintillators, respectively. R_1 and R_2 were set to 0.05 and 0.1 for all three scintillators.

^{a)}Electronic mail: jakob.larsson@biox.kth.se

¹S. W. Wilkins, T. E. Gureyev, D. Gao, A. Pogany, and A. W. Stevenson, “Phase-contrast imaging using polychromatic hard x-rays,” *Nature* **384**, 335–338 (1996).
²F. Pfeiffer, T. Weitkamp, O. Bunk, and C. David, “Phase retrieval and differential phase-contrast imaging with low-brilliance x-ray sources,” *Nat. Phys.* **2**, 258–261 (2006).
³U. Lundstrom, D. H. Larsson, A. Burvall, L. Scott, U. K. Westermark, M. Wilhelm, M. Arsenian Henriksson, and H. M. Hertz, “X-ray phase-contrast CO₂ angiography for sub-10 μm vessel imaging,” *Phys. Med. Biol.* **57**, 7431–7441 (2012).
⁴D. H. Larsson, U. Lundstrom, U. K. Westermark, M. Arsenian Henriksson, A. Burvall, and H. M. Hertz, “First application of liquid-metal-jet sources for small-animal imaging: High-resolution CT and phase-contrast tumor demarcation,” *Med. Phys.* **40**, 021909 (7pp.) (2013).
⁵J. M. Boone, *Handbook of Medical Imaging, Volume 1. Physics and Psychophysics* (SPIE, Bellingham, DC, 2000), pp. 64–65.
⁶V. V. Nagarkar, T. K. Gupta, S. R. Miller, Y. Klugerman, M. R. Squillante, and G. Entine, “Structured CsI(Tl) scintillators for x-ray imaging applications,” *IEEE Trans. Nucl. Sci.* **45**, 492–496 (1998).
⁷P. Kleimann, J. Linnros, C. Fröjd, and C. S. Petersson, “An x-ray imaging pixel detector based on a scintillating guides screen,” *IEEE Trans. Nucl. Sci.* **47**, 1483–1486 (2000).
⁸V. V. Nagarkar, S. V. Tipnis, V. B. Gaysinskiy, S. R. Miller, A. Karellas, and S. Vedantham, “New design of a structured CsI(Tl) screen for digital mammography,” *Proc. SPIE* **5030**, 541–546 (2003).
⁹J. T. Dobbins III, *Handbook of Medical Imaging, Volume 1. Physics and Psychophysics* (SPIE, Bellingham, DC, 2000), pp. 161–219.
¹⁰J. T. Bushberg, J. A. Seibert, E. M. Leidholdt, and J. M. Boone, *The Essential Physics of Medical Imaging*, 2nd ed. (Lippincott Williams & Wilkins, Philadelphia, PA, 2002), pp. 255–291.
¹¹E. Samei, “Image quality in two phosphor-based flat panel digital radiographic detectors,” *Med. Phys.* **30**, 1747–1757 (2003).
¹²W. Zhao, G. Ristic, and J. A. Rowlands, “X-ray imaging performance of structured cesium iodide scintillators,” *Med. Phys.* **31**, 2594–2605 (2004).
¹³T. T. Farman, R. H. Vandre, J. C. Pajak, S. R. Miller, A. Lempicki, and A. G. Farman, “Effects of scintillator on the modulation transfer function (MTF) of a digital imaging system,” *Oral Surg. Oral Med. Oral Pathol. Oral Radiol. Endod.* **99**, 608–613 (2005).
¹⁴K. W. Jee, L. E. Antonuk, Y. El-Mohri, and Q. Zhao, “System performance of a prototype flat-panel imager operated under mammographic conditions,” *Med. Phys.* **30**, 1874–1890 (2003).
¹⁵A. L. Goertzen, V. Nagarkar, R. A. Street, M. J. Paulus, J. M. Boone, and S. R. Cherry, “A comparison of x-ray detectors for mouse CT imaging,” *Phys. Med. Biol.* **49**, 5251–5265 (2004).
¹⁶E. Samei, M. J. Flynn, and D. A. Reimann, “A method for measuring the presampled MTF of digital radiographic systems using an edge test device,” *Med. Phys.* **25**, 102–113 (1998).
¹⁷K. A. Fetterly and N. J. Hangiandreou, “Effects of x-ray spectra on the DQE of a computed radiography system,” *Med. Phys.* **28**, 241–249 (2001).
¹⁸R. K. Swank, “Absorption and noise in x-ray phosphors,” *J. Appl. Phys.* **44**, 4199–4203 (1973).
¹⁹G. Lubberts, “Random noise produced by x-ray fluorescent screens,” *J. Opt. Soc. Am.* **58**, 1475–1483 (1968).
²⁰C. E. Dick and J. W. Motz, “Image information transfer properties of x-ray fluorescent screens,” *Med. Phys.* **8**, 337–346 (1980).
²¹See supplementary material at <http://dx.doi.org/10.1118/1.4948687> for a detailed derivation of the effective absorption efficiency and the number of visible-light photons generated per absorbed x-ray photon using a linear cascade model.
²²J. Yao and I. A. Cunningham, “Parallel cascades: New ways to describe noise transfer in medical imaging systems,” *Med. Phys.* **28**, 2020–2038 (2001).
²³S. Vedantham, A. Karellas, and S. Suryanarayanan, “Solid-state fluoroscopic imager for high-resolution angiography: Parallel-cascaded linear systems analysis,” *Med. Phys.* **31**, 1258–1268 (2004).
²⁴S. Hejazi and D. P. Trauernicht, “System considerations in CCD-based x-ray imaging for digital chest radiography and digital mammography,” *Med. Phys.* **24**, 287–297 (1997).
²⁵Proxvision, personal communication (www.proxvision.de).
²⁶I. Kandarakis, D. Cavouras, G. S. Panayiotakis, and C. D. Nomicos, “Evaluating x-ray detectors for radiographic applications: A comparison of Zn-SCdS:Ag with Gd₂O₂S:Tb and Y₂O₂S:Tb screens,” *Phys. Med. Biol.* **42**, 1351–1373 (1997).

- ²⁷G. W. Ludwig, "X-ray efficiency of powder phosphors," *J. Electrochem. Soc.* **118**, 1152–1159 (1971).
- ²⁸R. K. Swank, "Calculation of modulation transfer functions of x-ray fluorescent screens," *Appl. Opt.* **12**, 1865–1870 (1973).
- ²⁹N. Kalyvas, I. Valais, C. Michail, G. Fountos, I. Kandarakis, and D. Cavouras, "A theoretical study of CsI:TI columnar scintillator image quality parameters by analytical modeling," *Nucl. Instrum. Methods Phys. Res., Sect. A* **779**, 18–24 (2015).
- ³⁰D. Nikolopoulos, N. Kalyvas, I. Valais, X. Argyriou, E. Vlamakis, T. Sevvos, and I. Kandarakis, "A semi-empirical Monte Carlo based model of the detector optical gain of nuclear imaging scintillators," *J. Instrum.* **7**, P11021 (2012).
- ³¹C. W. E. van Eijk, "Inorganic scintillators in medical imaging," *Phys. Med. Biol.* **47**, R85–R106 (2002).
- ³²Hamamatsu, X-ray scintillator, 2009.
- ³³Hamamatsu, Fop—Fiber optic plates, 2013.